Plasma Physics and Controlled Fusion

PAPER • OPEN ACCESS

First observations of confined fast ions in MAST Upgrade with an upgraded neutron camera

To cite this article: M Cecconello *et al* 2023 *Plasma Phys. Control. Fusion* **65** 035013

View the article online for updates and enhancements.

You may also like

- Overview of new MAST physics in anticipation of first results from MAST Upgrade
J.R. Harrison, R.J. Akers, S.Y. Allan et al.
- Mitigation of MHD induced fast-ion redistribution in MAST and implications for MAST-Upgrade design
D.L. Keeling, T.R. Barrett, M. Cecconello et al.
- Energetic particles in spherical tokamak plasmas
K G McClements and E D Fredrickson

This content was downloaded from IP address 130.238.191.104 on 13/03/2023 at 09:30

OPEN ACCESS
IOP Publishing
Plasma Physics and Controlled Fusion
Plasma Phys. Control. Fusion **65** (2023) 035013 (16pp)
https://doi.org/10.1088/1361-6587/acb50c

First observations of confined fast ions in MAST Upgrade with an upgraded neutron camera

M Cecconello[1,2,*], I J Dolby[1], A Sperduti[2], J Rivero-Rodriguez[3], G Ericsson[2], I Fitzgerald[3], S Y Allan[3], J Voller[3], B Honey[3], B A Nizar[3], S D Elmore[3] and the MAST-U team[4]

[1] Department of Physics, Durham University, Durham DH1 3LE, United Kingdom
[2] Department of Physics and Astronomy, Uppsala University, Uppsala SE-751 05, Sweden
[3] CCFE, Culham Science Centre, Oxon OX14 3DB, United Kingdom

E-mail: marco.cecconello@durham.ac.uk

Received 12 October 2022, revised 11 January 2023
Accepted for publication 20 January 2023
Published 7 February 2023

Abstract

Spherical tokamaks are key to the successful design of operating scenarios of future fusion reactors in the areas of divertor physics, neutral beam current drive and fast ion physics. MAST Upgrade, which has successfully concluded its first experimental campaign, was specifically designed to address the role of the radial gradient of the fast ion distribution in driving the excitation of magneto-hydrodynamic (MHD) instabilities, such as toroidal Alfvén eigenmodes, fish-bones and long-lived mode, thanks to its two tangential neutral beam injection systems, one on the equatorial plane and one that is vertically shifted 65 cm above the equatorial plane. To study the fast ion dynamics in the presence of such instabilities, as well as of sawteeth and neo-classical tearing modes, several fast ion diagnostics were upgraded and new ones added. Among them, the MAST prototype neutron camera (NC) has been upgraded to six, equatorial sight-lines. The first observations of the confined fast ion behavior with the upgraded NC in a wide range of plasma scenarios characterized by on-axis and/or off-axis heating and different MHD instabilities are presented here. The observations presented in this study confirm previous results on MAST but with a higher level of detail and highlight new physics observations unique to the MAST Upgrade. The results presented here confirm the improved performance of the NC Upgrade, which thus becomes one of the key elements, in combination with the rich set of fast ion diagnostics available on the MAST Upgrade, for a more constrained modeling of the fast ion dynamics in fusion reactor relevant scenarios.

Keywords: MAST Upgrade, fast ions, neutron diagnostics

(Some figures may appear in colour only in the online journal)

[4] Harrison *et al* 2019 *Nucl. Fusion* **59** 11201.
[*] Author to whom any correspondence should be addressed.

Original Content from this work may be used under the terms of the Creative Commons Attribution 4.0 licence. Any further distribution of this work must maintain attribution to the author(s) and the title of the work, journal citation and DOI.

 © 2023 The Author(s). Published by IOP Publishing Ltd

1. Introduction

Fast ions are a key ingredient in achieving reactor relevant conditions, contributing to both plasma heating and the non-inductive current drive of present day and future fusion devices, such as ITER and DEMO [1, 2]. It is well known that fast ions, in addition to these beneficial contributions, can drive magneto-hydrodynamic (MHD) instabilities which reduce the overall confinement of the fast ions, leading to their redistribution and losses with a subsequent reduction in plasma performance and possible damage to the first wall if lost fast ions end up in localized areas. Typical examples of fast ion-driven instabilities are toroidal Alfvén eigenmodes (TAEs) and fishbones (FBs); specific to spherical tokamaks, the long-lived mode (LLM) instability is also responsible for the suppression of fast ion population. In addition, fast ions are also susceptible to instabilities which depend, instead, on the plasma equilibrium and scenario: typical examples are sawteeth (ST) and neo-classical tearing modes (NTMs, which have been observed to be seeded by both fast ion instabilities and ST). The design of the operating scenarios for future fusion reactors is based on the validation of the descriptive and predictive capabilities of the numerical codes used to model aspects of the linear and non-linear interactions between fast ions and MHD instabilities via comparison with experimental observations. Spherical tokamaks, in particular, thanks to the lower magnetic field and neutral beam injection (NBI) external auxiliary heating systems with energies up to 60–100 keV, can explore plasma regimes not readily accessible to present day conventional tokamaks in which the fast ions are super-Alfvénic, similar to what is predicted for α-particles in ITER.

MAST Upgrade [3] (MAST-U in brief), which was designed to address, among other objectives, the interplay between MHD instabilities, fast ions and neutral beam current drive, has successfully concluded its first experimental campaign providing a wealth of new results [4]. MAST-U, although it retains the same aspect ratio ($R/a = 0.85/0.65 \approx 1.3$) of MAST, has new capabilities, including a set of new poloidal field coils for highly flexible plasma shaping (including different divertor configurations, such as the Super-X divertor), a higher toroidal field (up to 0.85 T), higher plasma current (up to 2 MA) and longer pulses (up to 5 s) and a very flexible heating and current drive system. This flexibility is achieved by having one NBI depositing fast ions on-axis and a second one off-axis, 65 cm above the equatorial plane [3]: in MAST, both NBIs were on-axis [5, 6]. The goal with this on-axis and off-axis combination, aided by plasma density control, is to achieve scenarios with substantial non-inductive current drives and heating with minimal fast ion losses. Its justification is based on (a) the theoretical predictions of a direct proportionality between the radial gradient of the fast ion distribution and the driving of MHD instabilities detrimental to fast ion confinement, and on (b) the experimental observations of such predictions in MAST [7]. In order to study the rich fast ion physics in MAST-U, several fast ion diagnostics have been upgraded and new ones added, such as the fast ion D-alpha system, a fast-ion loss detector (FILD) [8], a solid state neutral particle analyzer and a charged fusion product detector [9]. In particular, the prototype neutron camera (NC) [10] has been upgraded to the NC Upgrade (NCU) with six sight-lines (all on the equatorial plane) [11].

The aim of this study is to showcase the improved performance of the NCU (described in section 2) and its first experimental observation and preliminary modeling of fast ion dynamics in a wide range of MAST-U scenarios with on-axis and off-axis NBI heating (section 3) and in the presence of ST, TAEs, FBs and NTMs (section 4). Although the focus is on the NCU instrument, other plasma diagnostics relevant to the interpretation of fast ion dynamics are used. The electron density and temperature profiles are measured by the core Thomson scattering system with 130 radial points between 0.25 and 1.45 m and with a time resolution of 5 ms [12]. The global neutron rate is measured by a fission chamber (FC) with a sub-millisecond time resolution. The plasma rotation and ion temperature are inferred from the measurement of the C^{5+} impurity rotation velocity and temperature profiles by the charge-exchange recombination spectrometer with a time resolution of 5 ms [13]. The magnetic perturbation fluctuations are measured by a set of high sampling frequency (10 MHz) Mirnov pick-up coils (OMAHA) [14]. Fast ion losses are measured by FILD using a slow and a fast camera with a frame rate of 23 Hz and 4 MHz respectively: fast camera data are not available for all the plasma discharges discussed here. Finally, the neutron emissivity profiles measured by the NCU all have a time resolution of 1 ms and a spatial resolution of 10 cm. A direct comparison of the findings presented here with other fast ion diagnostics is part of a future study since not all the systems were fully operational during the first MAST-U experimental campaign. The quantitatively accurate modeling of the plasma discharges presented here is hampered by the lack of measurement of the plasma effective charge $Z_{\rm eff}$ and by a large uncertainty in the energy fractions of the on-axis NBI system. The TRANSP/NUBEAM [15, 16] simulations presented in this study all assume a flat radial profile of the effective charge with $Z_{\rm eff} = 1.5$ and full- and half-energy fractions of approximately 44/44 for the on-axis NBI (instead of 78/16) and 78/16 for the off-axis NBI. The energy fractions for the on-axis NBI system have been inferred from spectroscopic measurements of the total radiated power and from comparisons between predicted neutron rates and emissivities together with those measured by the FC and NCU. A detailed analysis of this is the focus of a separate study. Finally, real-time control of the electron density was not implemented during the first MAST-U experimental campaign: this is quite relevant to the dynamics of fast ions since it determines where the fast ions are deposited and thus the radial gradient of the fast ion distribution, a quantity that controls the driving of fast ion instabilities.

2. The upgraded NC

A cut-away CAD model of the NCU is shown in the left panel of figure 1 where the detectors and the lines of sight are visible inside the lead and high-purity, high density polyethylene shielding. The right panel of the same figure shows

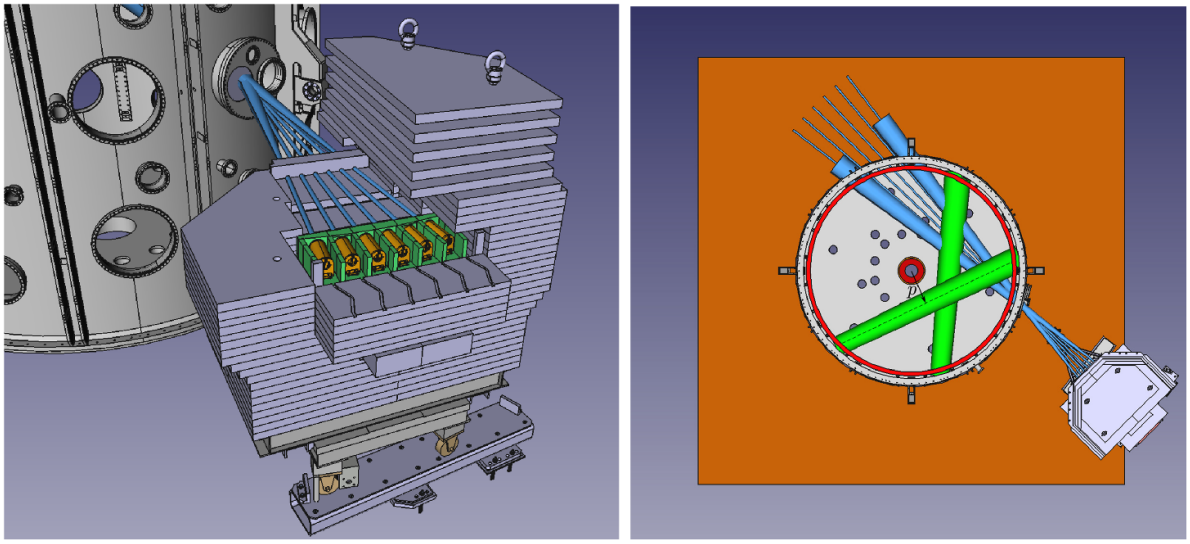

Figure 1. Left panel: cut-away of the NCU showing the six detectors (in orange) and the fields of view (in blue) inside the lead shield (in green) and the high density polyethylene shield (in dark gray) in relation to the MAST-U vessel (gray); the special thin flange is also visible. Right panel: top view of the NCU sight lines together with the field of view of the outermost two (in blue) and of the footprint of the two NBIs with the off-axis one above the on-axis one (in green). The black dashed line indicates the axis of the off-axis NBI system with an impact parameter $p = 0.7$ m (black arrow). The same definition of the impact parameter is used to characterize the lines of sight for each detector.

a top view of the NCU in relation to the MAST-U vessel and the footprint of the NBI injectors; also shown are the fields of view of the outermost channels. The main differences between the NCU and the NC are: (a) six lines of sight on the machine equatorial plane ($Z = 0$ m) instead of two measuring the neutron emissivity with a spatial resolution of 10 cm and with impact parameter $p \in [0.6, 1.1]$ m; (b) tangential view in the co-NBI injection direction instead of counter-NBI injection for the NC; (c) cylindrical instead of rectangular collimators with a cross-sectional area of approximately 7 cm^2 instead of 10 cm^2 (reduced in view of the expected doubling of the NBI input power in the future); (d) improved shielding against γ-rays; (e) cylindrical detectors instead of rectangular ones (but with the same thickness of 1.5 cm) with improved energy resolution and pulse shape discrimination capabilities; and (f) individual magnetic shielding instead of a common shielding for all detectors. As in the NC, the NCU uses detectors based on EJ-301 liquid scintillating material coupled to a photomultipier tube (PMT) with an embedded ^{22}Na γ-ray source for calibration and an optical fiber connected to a pulsed LED at 5 kHz for monitoring purposes. The data acquisition system is also the same with six channels each operating at 250 MSamples/s with 14-bit resolution and 256 MB on-board memory. The NCU retains the scanning capability of the NC although it has not been implemented yet: nevertheless, as shown in the following sections, the simultaneous measurement of the neutron emissivity at six impact parameters has proven sufficient to capture most of the relevant fast ion dynamics. A detailed description of the design choices and the performance of the NCU in laboratory settings can be found in [11]. In this section, instead, its performance during plasma operations is briefly presented. Figure 2 shows the performance of the NC and NCU in similar plasma scenarios in MAST and MAST-U, respectively. characterized by on-axis NBI heating only. One key improvement of the NCU, in addition to those detailed in [11], has been the suppression of the 2.2 MeV γ-rays generated by the thermal neutron capture by the hydrogen nuclei of the polythene shielding as a result of an improved design of the lead shielding. This results in a lower load on the data acquisition system as well as an improvement in the pulse shape discrimination between neutron and γ-rays events. The left panel of this figure shows the ratio of the count rates between γ-rays and neutrons in the time interval 0.25–0.30 s as measured by the NC and NCU for plasma discharges #29904–#29910 for MAST and #45006 for MAST-U respectively. The overall reduction in the γ-rays/neutron count rate ratio is approximately equal to 7.5 for $p \leqslant 1$ m and 5 for larger p. This significant improvement, thanks to point (d) above, allows us to extend the data acquisition to longer (>1 s) plasma discharges without requiring an upgrade of the on-board memory. This, in combination with point (e), also results in an improved discrimination between neutrons and γ-rays. The γ-ray/neutron count rate ratio increases at larger p values due to MAST-U plasmas being characterized by a higher elongation and triangularity compared to MAST. The neutron emissivity region is thus narrower, giving fewer neutron counts already at $p \geqslant 1$ (the flux of γ-rays reaching the detectors is approximately the same for all detectors since it is due to thermal neutron capture in the shielding surrounding the detectors). The improved energy resolution of the NCU is clearly seen in the right panel of figure 2 where the recoil proton pulse height spectrum, integrated over the entire plasma discharge, is shown in terms of the electron-equivalent energy for pulses #29906 and #45006: the 'edge' in the pulse height spectrum, due to the full energy transfer (head-on collision) between a 2.5 MeV neutron and a hydrogen nucleus and corresponding to an electron equivalent energy of approximately 0.7–0.8 MeV, is much sharper for the

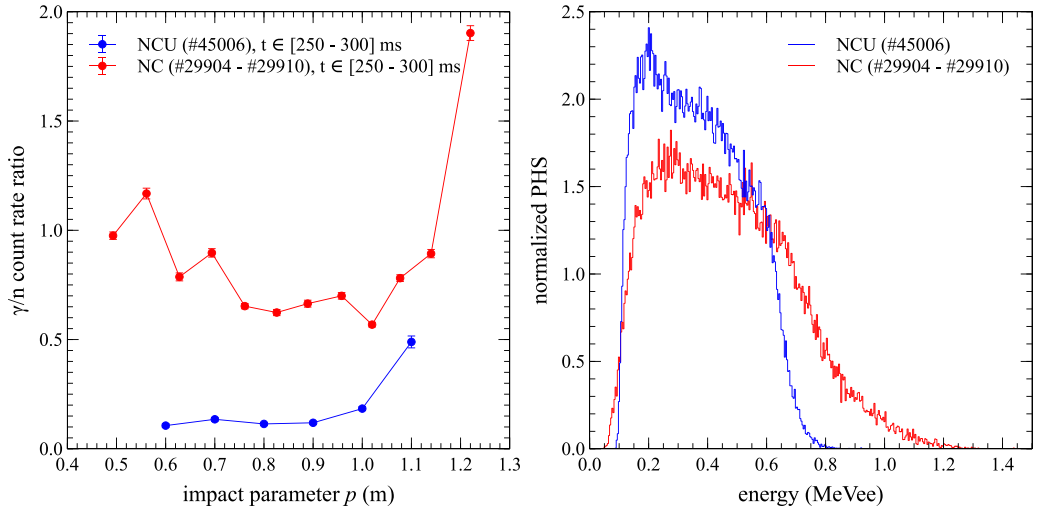

Figure 2. Left panel: comparison of the ratio of the γ-rays and neutron count rates for the NC (using multiple plasma discharges, in red) and the NCU (# 45006, in blue) as a function of the impact parameter in the time interval 0.25–0.3 s. Right panel: comparison of the normalized, profile-averaged recoil proton PHS for the same pulses as the left panel.

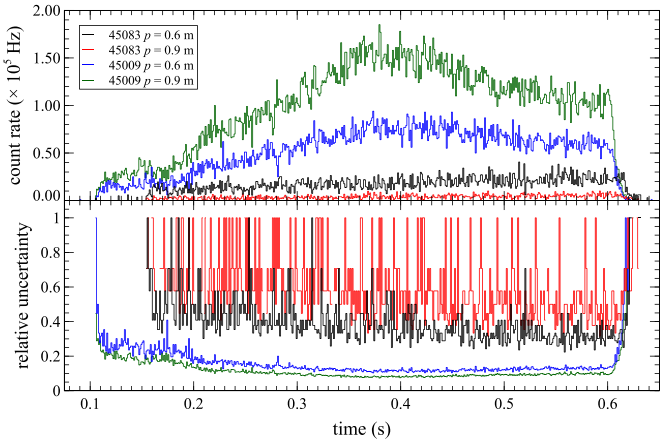

Figure 3. Top panel: neutron count rate for two different impact parameters ($p = 0.6$ m, inboard, and $p = 0.9$ m, core) for MAST-U pulses #45009 (on-axis NBI only) and #45083 (off-axis NBI only). Bottom panel: relative uncertainty.

NCU. The location of the midpoint of the 'edge' is located at different energies: this is a consequence of the relative direction of observation with respect to the NBI injection, as mentioned in point (b) above. Finally, figure 3 shows the relative uncertainty in the count rates with an integration time of 1 ms for MAST-U pulse #45009 (on-axis NBI only) and #45083 (off-axis NBI only) in the plasma core ($p = 0.9$ m) and on the inboard side ($p = 0.6$ m). For pulse #45009, the relative uncertainty in the count rate is approximately 10% for all impact parameters. On the other hand, for pulse #45083, the relative uncertainty is approximately 40% and 60% at the inboard side and in the plasma core, respectively. The reason for this large uncertainty for pulse #45083 is due to the very low count rate observed in plasma scenarios with off-axis heating only. In such cases, the neutron rate is typically a factor 10 lower than plasma scenarios with on-axis heating for the same global plasma parameters (density and temperature) and NBI input power and energy. In addition, off-axis NBI auxiliary heating results in hollow neutron emissivity profiles (as discussed in more detail in the next section) with peak emissivity on the inboard side. In summary, the NCU has met all its design specifications and it is ready to be exploited for fast ion studies, as the results in the following sections demonstrate.

3. On- and off-axis NBI heating

A systematic optimization of the NBI injection geometry for heating, non-inductive current drive and reduced fast ion redistribution using TRANSP/NUBEAM in predictive mode is described in detail in [17]. The predicted peaked and hollow profiles of the fast ion density [3] have been experimentally confirmed to match TRANSP/NUBEAM predictions, as shown in figure 4. The pulses used for this comparison, #45238 (off- and on-axis NBI) and #45083 (off-axis NBI only), were selected since they exhibited time intervals free of the typical MHD instabilities affecting fast ions, such as FBs, TAEs, LLMs, ST and NTMs. Apart from the different NBI heating systems, these two pulses are very similar (L-mode plasmas in a double-null divertor configuration with a 600 kA plasma current) as shown in figure 10. In MAST-U, MHD-quiescent plasmas are very common in plasma scenarios with off-axis NBI heating only: a partial explanation might be due to the plasma elongation during the first MAST-U experimental campaign ($\kappa \approx 2.1$, [4]) being lower than the design values for MAST-U scenarios ($\kappa \approx 2.5$), resulting in off-axis fast ions being born close to the last closed-flux surface. This implies that the background plasma density and temperature is lower than the designed values, reducing the beam-thermal fusion reaction rate, which is approximately 90% of the total neutron emission. In addition, fast ions with large Larmor radii and orbit widths born closer to the last close flux surface than was intended make them susceptible to prompt CX losses, further reducing the beat-thermal reactivity. On the other hand, most

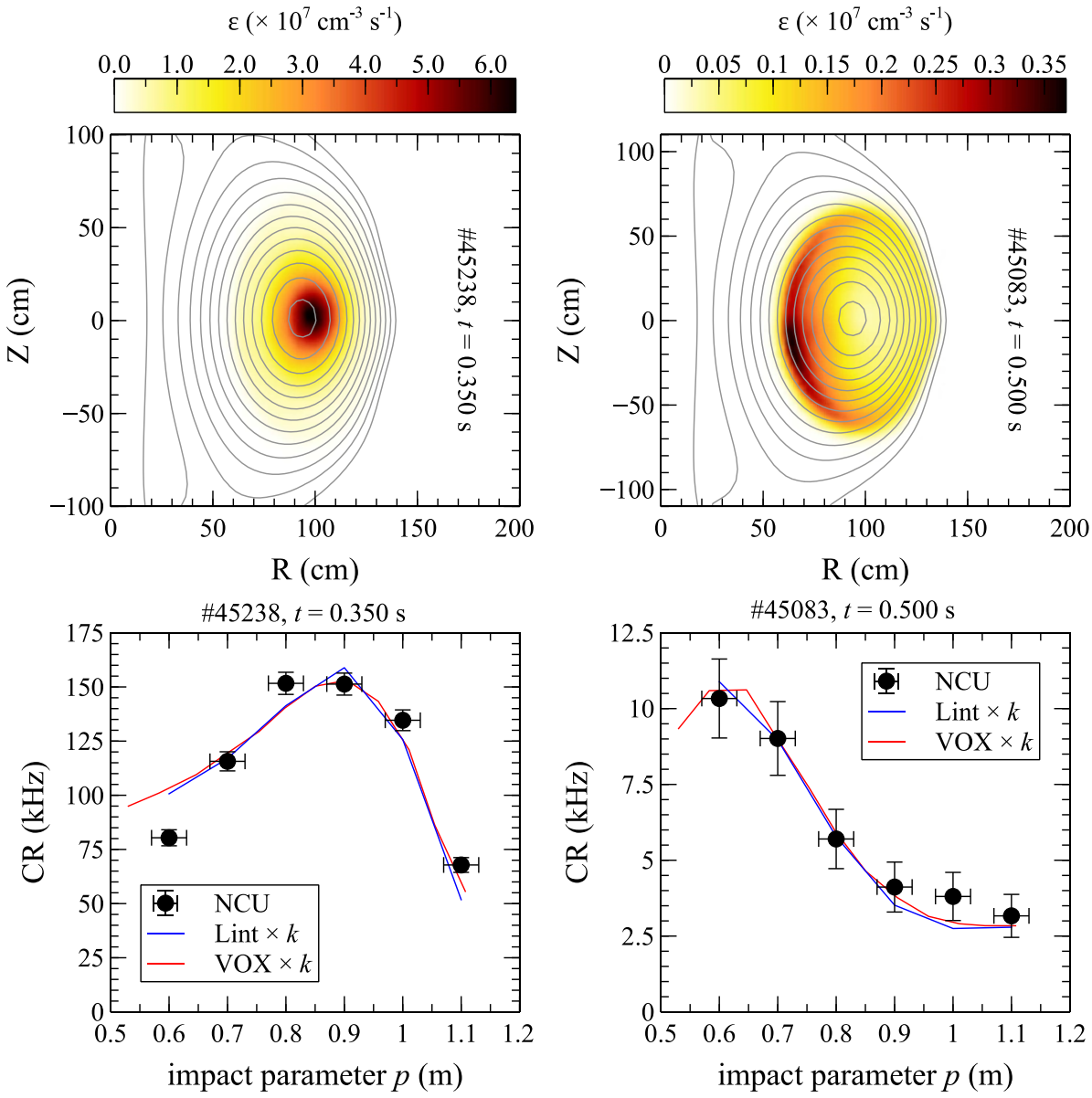

Figure 4. Top row: TRANSP/NUBEAM calculated neutron emissivity for pulses #45238 at $t = 0.350$ s with off- and on-axis NBI heating (left panel) and #45083 at $t = 0.500$ s with off-axis NBI heating only. Bottom row: comparison between NCU measurements (black solid circle) and predictions based on the neutron emissivities shown above using simple line of sight integrals (lint, blue line) and full 3D field of view geometry (VOXels, red line). The scaling factor is $k = 0.4$.

plasma discharges in which fast ions are deposited on-axis are characterized by an initial phase with TAEs and FBs followed by low frequency NTMs (5–10 kHz) and when $q(0) < 1$ ST is observed. Extended time intervals of MHD-quiescent plasmas with on-axis NBI heating have rarely been observed in MAST-U. The predicted NCU profiles are based on TRANSP/NUBEAM simulations of the fast ion distribution and the non-flux averaged neutron emissivity at selected times [18], assuming no fast ion anomalous diffusion. Although the shape of the predicted NCU emissivity profiles is quite well reproduced, a scaling factor $k \approx 0.4$ is necessary in both cases to match them to the absolutely calibrated NCU measurements. This scaling factor is smaller than the one observed in MAST ($k \approx 0.65$) [19]. The reason for this difference is not entirely understood. A possible explanation might be related to steeper gradients in the magnetic field in MAST-U due to larger elongations than in MAST (for which $\kappa \approx 1.9$), even when the finite Larmor radius correction is included in the TRANSP/NUBEAM simulations, as was the case here. The condition for the validity of the guiding center approximation (used in TRANSP/NUBEAM) is usually expressed as $r_L|\nabla B|/B \ll 1$ where r_L is the Larmor radius and B is the total magnetic field. This condition can be rewritten in terms of the fast ion energy E and pitch λ as $\sqrt{2mE/q^2}\sqrt{1-\lambda^2}|\nabla B|/B^2 \ll 1$ where m and q are the mass and charge of the fast ions. Figure 5 shows the comparison between the quantity $r_L|\nabla B|/B$ calculated for MAST (#29904, solid line) and MAST-U (#45006, dashed line) equilibria at $t = 240$ ms along the major radius for $Z = 0$ m for fast ions

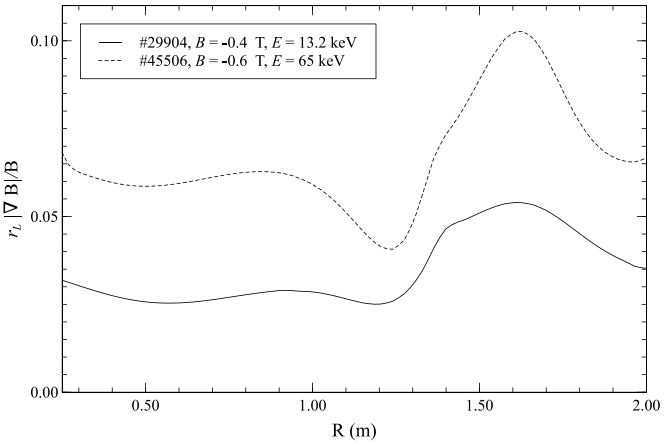

Figure 5. Example of the relation $r_L|\nabla B|/B$ calculated for MAST (#29904, solid line) and MAST-U (#45006, dashed line) equilibria at $t = 240$ ms along the major radius for $Z = 0$ m for fast ions with equal $\sqrt{E}/B^2$ and with $\lambda = -0.8$.

with equal $\sqrt{E}/B^2$ and with $\lambda = -0.8$ (the predominant pitch for fast ions injected on-axis). These two plasma discharges are quite similar, as discussed later in this section. As can be seen, in MAST-U, the condition $r_L|\nabla B|/B \ll 1$ is less favorable in MAST-U than in MAST. The limits of the guiding center approximation for spherical tokamaks were explored in MAST, where it was found that a full gyro-orbit modelling of the fast ions using ASCOT [20, 21] resulted in a better agreement between predicted and observed neutron camera measurements [22].

Figure 6 shows a comparison between the fission chamber and the NCU time traces and the total neutron yield. The neutron rates have been normalized to the total yield: for the NCU, the sum of the neutron rates for all six channels is used. The time traces shown on the left panels of figure 6 are representative of plasma scenarios with on-axis (#45009) or off-axis (#45083) only NBI-heated discharges. In the case of off-axis NBI heating, the time evolution of the FC and NCU agree very well, while for on-axis NBI heating, deviations between the two are observed. This is due to the fact that most of the plasmas with off-axis NBI heating are MHD-quiescent (apart from low frequency modes with little impact on the fast ion population, as described later), while MHD instabilities such, as TAEs, FBs and NTMs, are present when the on-axis NBI is used, leading to localized fast ion redistribution which is captured by the NCU but not by the FC. Also shown in figure 6 is the scaling between the total yield for the NCU (again summed over all six channels) and the FC: good linearity is observed, although the scaling factor is quite different for off-axis NBI-heated discharges compared to plasma discharges with on-axis (with or without off-axis) NBI heating. The different scaling for the off-axis scenarios is due to the NCU's localized view of the plasma core, while the maximum of the neutron emissivity is below the equatorial plane, as shown in the top right panel of figure 4.

Finally, figure 7 shows the neutron count rate comparison between two similar plasma scenarios measured with the NC in MAST and the NCU in MAST-U. The selected MAST scenario is a high density, MHD-quiescent scenario referred to as S1 in [19], characterized by a plasma current of approximately 800 kA, a core electron temperature of 1 keV and a core electron density of 6×10^{19} m^{-3}; the magnetic field on the axis is ≈ -0.4 T. The measured NC profile shown in figure 7 is the combination of six similar plasma pulses in which the NC position was changed to scan the entire plasma region from inboard to outboard. The selected MAST-U plasma discharge #45006 is characterized by a plasma current of 750 kA, a core electron temperature of 1 keV and a similar core electron density of 4×10^{19} m^{-3} and has a magnetic field on the axis of ≈ -0.6 T. Plasma discharge #45006 is not as MHD-quiescent as the S1 scenarios: weak TAEs and a $(m,n) = 2/1$ NTM are present in the early phase of the plasma discharge (for $t < 0.3$ s and $t < 0.38$ s respectively), during which the neutron rate is still growing, thus suggesting that the fast ion redistribution, if present, does not too strongly affect the fast ion population. Only on-axis NBI auxiliary heating was used in both cases, with an injection power and energy of 1.5 MW/60 keV and 1.3 MW/65 keV for #29904 and #45006, respectively, but with the main differences being that the full- and half-energy fractions in MAST were 78/16 rather than 44/44. The velocity averaged cross section $<\sigma v>$ in the central plasma region of the two scenarios for the full-energy fast ions is similar (1.8×10^{-24} m^3 s^{-1} and 2.1×10^{-24} m^3 s^{-1} respectively), resulting in similar beam-thermal reaction rates. When correction factors for the different collimation geometry of the NC and NCU and energy fractions in MAST and MAST-U are taken into account, the two profiles are comparable, with the exception at the outboard side ($p > 0.9$ m): the lower magnetic field and elongation in #29904 result in broader fast density profiles on the outboard side due to the large fraction of trapped particles in this region. This relatively good agreement supports the indirect evidence discussed earlier for the full- and half-energy fractions of the on-axis NBI system to be closer to 44/44 than to 78/16.

4. Observations of fast ion redistribution and losses

In this section, the preliminary results of the fast ion dynamics in the presence of different MHD instabilities observed during the first MAST-U experimental campaign are reported, showcasing the improved capabilities of the NCU.

4.1. ST

The impact of ST on fast ions on spherical tokamaks has been the subject of extensive studies [23–27] where the interested reader can find detailed discussions regarding the different behaviors of passing and trapped fast ions and the TRANSP/NUBEAM simulation of the associated loss of fast ions using the Kadomtsev and Porcelli models. More recently, a reduced model for the transport of fast ions by ST has been specifically developed [28] which enabled a more nuanced interpretation of the experimental observations on National Spherical Torus Experiment (NSTX). The initial results are

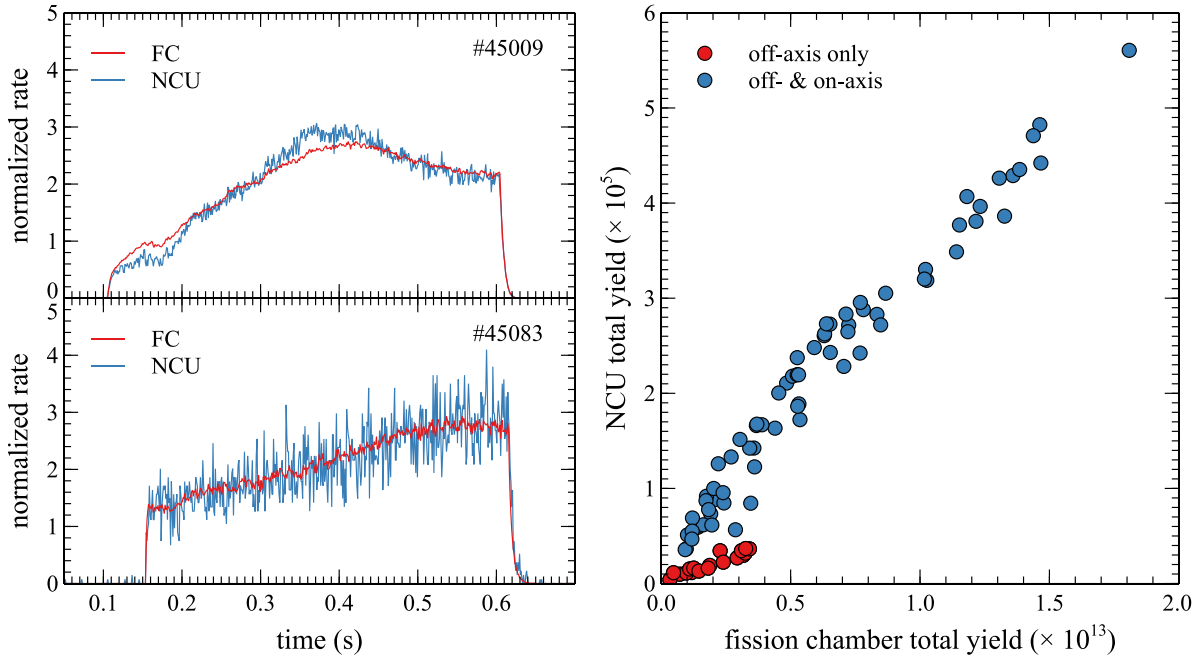

Figure 6. Left panel: normalized neutron rate measured by the fission chamber (red) and by the NCU (red) for plasma discharges with an on-axis only (#45009, top panel) and an off-axis only (#45083, bottom panel). Right panel: NCU total neutron yield versus the FC yield for plasma discharges with only off-axis NBI heating (red circle) and with on-axis (with or without off-axis) NBI heating (blue circles): each point represents a plasma discharge.

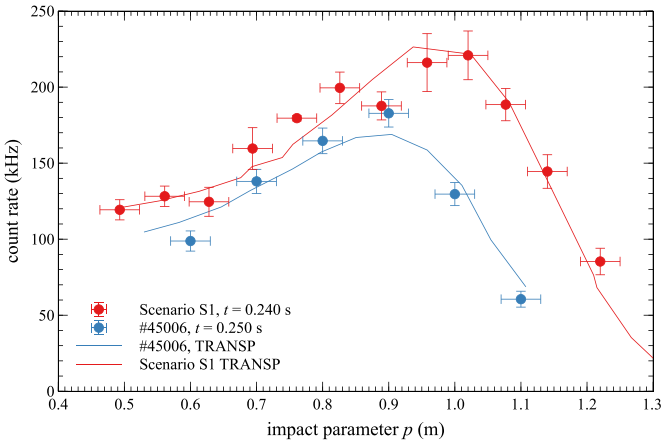

Figure 7. Comparison between neutron count rate profiles observed (solid circles) and predicted by TRANSP/NUBEAM (solid lines) for two similar plasma scenarios in MAST with the NC (scenario S1, in red) and in MAST-U with the NCU (#45006, in blue).

encouraging but further validationin particular, on other STs, such as MAST-U, is required. This, however, is left to future work: here, instead, the focus is limited to the first experimental observation of ST in MAST-U. Figure 8 shows the typical signature of ST in the core electron temperature, density, and neutron rates, and the corresponding profiles for plasma discharge #45031, an L-mode plasma in a double null configuration with a conventional divertor and with a flat-top plasma current of 450 kA and additional auxiliary heating of 1.5 MW provided by the on-axis NBI. The drop in the fast ion population at each sawtooth crash, inferred from the neutron measurements, is between 40% and 50% across the entire profile, in agreement with previous observations in MAST [23]. This is confirmed by FILD observations with the slow camera shown in the 5th panel on the left of figure 8 as magenta solid circles, which indicates an increase in the losses during the ST period. A noteworthy difference is the high field side peaking of the neutron count rate profile after the sawtooth crash, which was not observed in MAST: a possible explanation for this is that the scenario presented here is quite different from the one studied in MAST in terms of plasma current, density and NBI power.

In addition to the more traditional ST, an instability resembling the sawtooth but affecting only the thermal and fast ions in the core has been observed in MAST-U. An example is shown in figure 9: plasma discharge #45212 has a flat-top I_p of 750 kA, a total input NBI power of 3 MW (on-axis and off-axis) in which $q(0) < 1$ for $t > 0.3$ s (first panel of the top left figure). The line integrated electron density, the core electron and C^{5+} temperatures are shown in the second panel (note that the C^{5+} temperature measurements are available only when the on-axis NBI is applied). A closer look at the time trace of the neutron rate shown in the third panel of the top left figure is shown in the bottom left figure, together with the core temperature of the impurity ion C^{5+} at $r = 0.98$ m and the spectrogram of the OMAHA. Sudden bursts of MHD activity are seen at regular intervals with a frequency range extending from 5–100 kHz, a signature normally associated with ST. The bursts occur on a timescale of approximately 1 ms and the root-mean square value of the perturbation is a factor 10 smaller than for ordinary ST in MAST-U. In correspondence with these bursts, drops of about 5% in the neutron rates and of about 15% in the

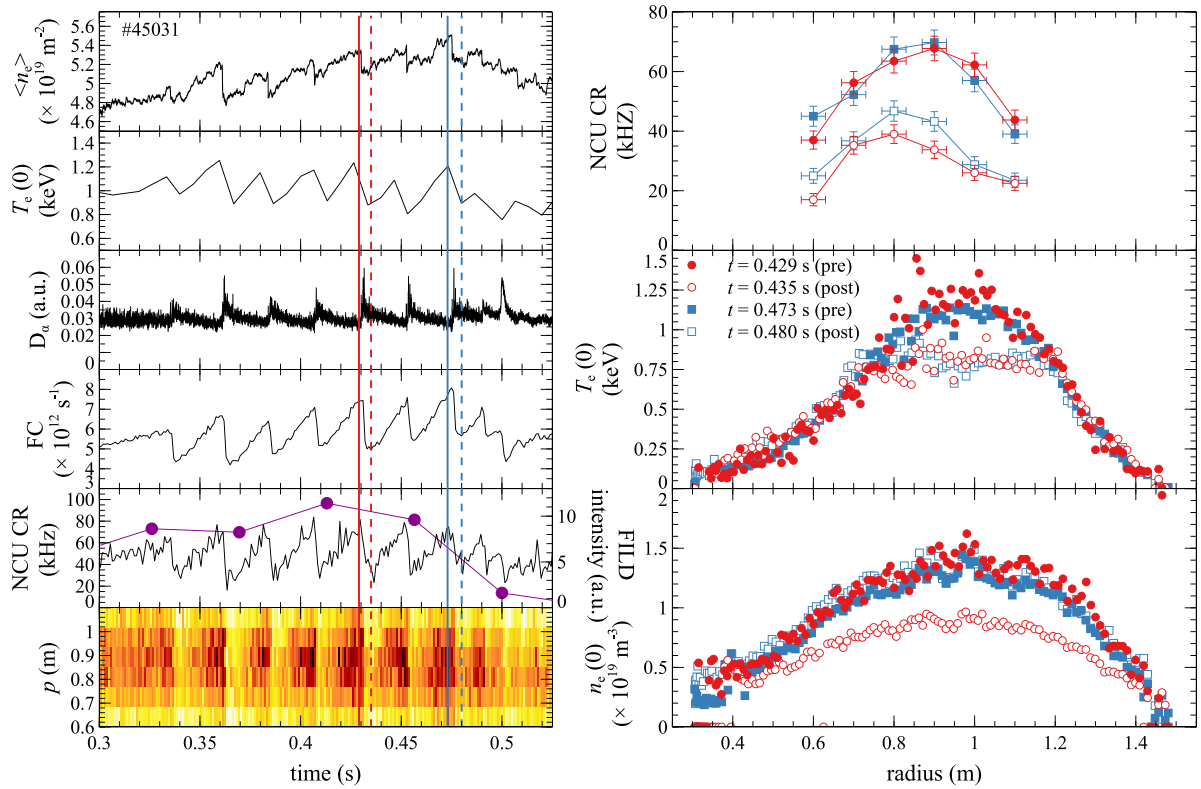

Figure 8. Sawteething plasma discharge #45031. Left figure, from top-to-bottom: line integrated density, core electron temperature, edge D_α signal, FC neutron rate, NCU neutron count rate for $p = 0.9$ m together with the FILD slow camera count rate (magenta solid circles) and NCU neutron count rate profile. Right figure: profile before and after two sawtooth crashes as observed by the NCU (top panel) and Thomson scattering (electron temperature and density, middle and bottom panels).

C^{5+} core temperature are observed compared to the pre-burst values. The radial profiles of the electron temperature and density, the C^{5+} temperature and the NCU neutron count rate before and after the MHD burst at $t = 0.407$ s are shown in the right panels of figure 9. The electron temperature and density profiles, measured at $t_{pre} = 0.4049$ s and $t_{post} = 0.4097$ s, are unaffected by this MHD burst or, if affected, the resulting change is smaller than the fluctuations in the data in the core region of the plasma. On the other hand, the C^{5+} temperature ($t_{pre} = 0.405$ s and $t_{post} = 0.410$ s) and the fast ion population ($t_{pre} = 0.405$ s and $t_{post} = 0.408$ s) in the core of the plasma are reduced by about 20% and 25%, respectively, (and about 10% across the entire profile). The sudden reduction in the neutron rate resembles what happens during a sawtooth, apart from the fact that the losses in this case are limited to the central region for $p \in [0.7, 0.8]$ m instead of affecting a large part of the plasma core. No fast ion losses from the edge region have been observed by the FILD, as shown in figure 9, which is consistent with the NCU results. The absence of a change in the electron temperature, however, is puzzling, assuming that these bursts are micro-ST (ST with no change in the electron density in STs is not uncommon); unfortunately, no soft x-ray signals were available for this pulse. In addition, a causal relation between the reduction in the fast ion population and in the C^{5+} temperature is unclear since the latter does not occur at each burst. The bursts occur on a timescale that is much faster than the fast ion slowing down time (approximately 120 ms in the core) and any reduction in the thermal ion temperature due to the loss of fast ions should be seen first in the electron temperature.

4.2. TAEs, FBs and LLMs

Examples of typical fast ion dynamics in MAST-U in the presence of TAEs, FBs and LLMs are presented in this section. TAEs are studied in pulse #45238, an L-mode plasma in a double null configuration with flat-top $I_p = 600$ kA, $P_{NBI} = 3$ MW, an average line integrated density $< n_e >= 1 \times 10^{20}$ m^{-2} and a core electron temperature of approximately 1 keV. TAEs are present in the early phase of the discharge ($t < 0.26$ s) in which the magnetic field on-axis is 0.54 T and the safety profile on-axis is decreasing from $q(0) = 3$ to $q(0) = 1.3$. Under these conditions, the fast ions deposited by both NBIs are super-Alfvénic with $v_{fi} \approx 2.5 \times 10^6$ m s^{-1}, whereas the Alfvén velocity is $v_A < v_{fi}$ everywhere in the plasma with $v_A \approx 1.5 \times 10^6$ m s^{-1} in the core. As a result, Alfvén waves can be excited via the resonance $v_{fi,||} = v_A$. A second pulse, #45083, in the same plasma scenario but with only off-axis heating, is used for comparison: in this case, the off-axis NBI has a higher injection energy of 72.5 keV and it is applied later into the pulse compared to #45238. The global traces for these two pulses are shown in figure 10. Two striking features characterize these plasma discharges. The first one is that with off-axis heating, the neutron rate from the off-axis

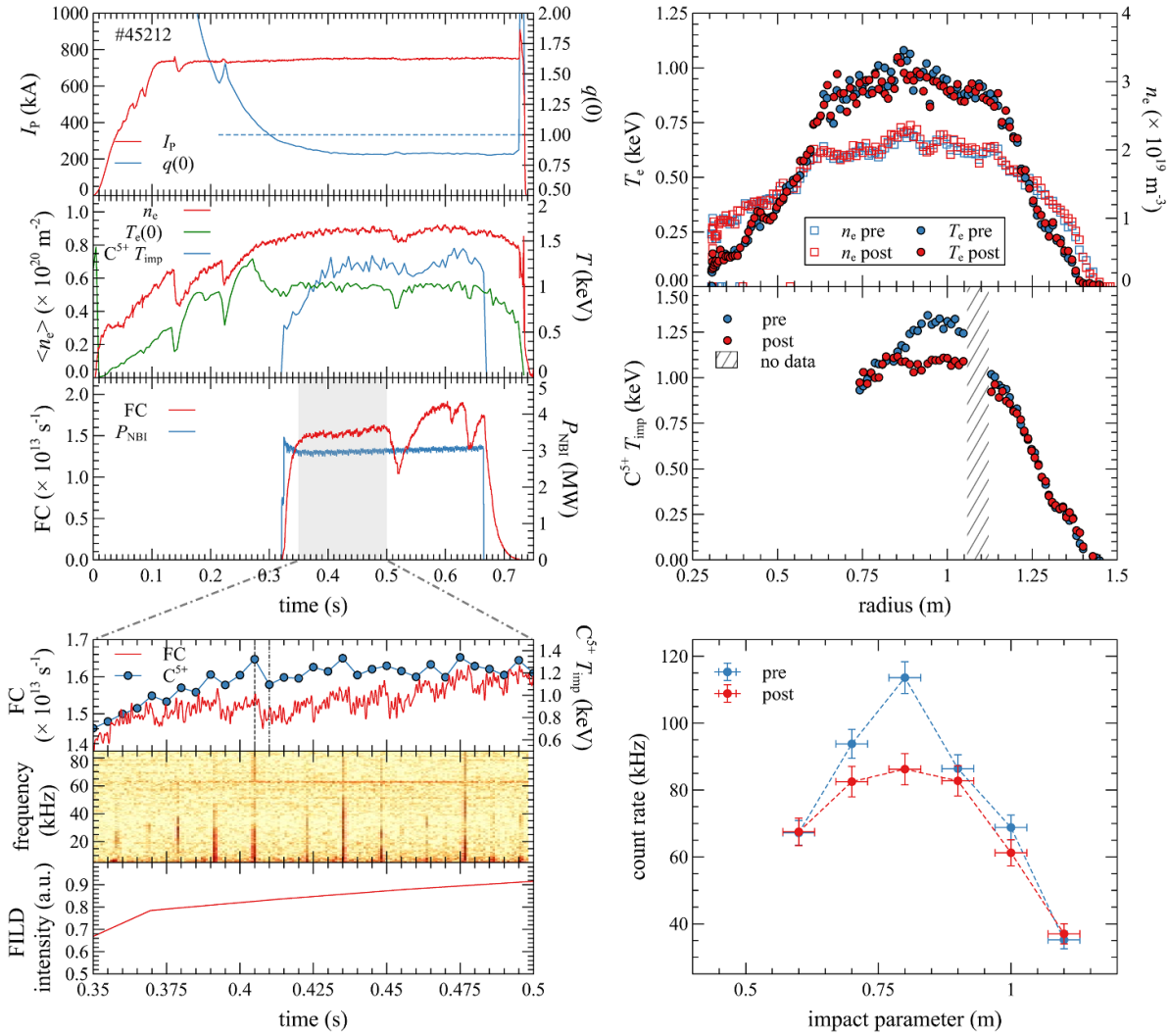

Figure 9. Plasma discharge (#45212). Top left panel, from top-to-bottom: plasma current and on-axis safety factor, line integrated electron density and core electron and C^{5+} temperatures, total NBI input power and FC neutron rate. Bottom left panel: zoomed in time window of the FC neutron rate with the core temperature of the impurity ion C^{5+} at $r = 0.98$ m, OMAHA pick-up coil spectrogram and FILD count rate. Right panels, radial profiles before and after the micro-sawtooth crash at $t = 0.407$ s for the electron temperature and density, the C^{5+} temperature and the NCU neutron count rate profile.

NBI-heated plasmas is approximately 1/10th of the neutron rate from the on-axis one (the thermal neutron rate is negligible in MAST-U). This has been confirmed independently by both the FC and the NCU, as shown in figure 6. Secondly, the MHD activity is completely different with pulse #45083 being MHD-quiescent, while #45238 is characterized by small amplitude TAEs followed by larger, bursting-like TAEs. A closer look at this bursting phase is presented in figure 11, showing TAEs chirping from an initial frequency of about 85 kHz down to 65 kHz, which is compatible with the expected central frequency of the toroidicity-induced gap in the shear Alfvén continuum of 80 kHz at the radial location, equal to half the minor radius, where TAE's eigenfunctions usually have the largest amplitude. During each burst, the fast ions are slightly redistributed from the outboard to the inboard side, as shown by the NCU neutron rate profiles in the right panel of figure 11, but no bursting loss of fast ions is observed (the term 'slightly' is used here to mean that the measured profiles are within the experimental uncertainty). The lack of loss of fast ions is also confirmed by FILD measurements. This is further confirmed by the lack of spikes in the edge D_α photon recombination emission, as shown in the left bottom panel of figure 11. These observations suggest that the radial gradient of the fast ion distribution is not sufficiently large to cause bursting fast ion losses, although a low level, continuous loss of fast ions cannot be excluded during the entire time interval in which the TAEs are observed (approximately between 0.15 s and 0.26 s). It is also worth noting that in this pulse, the line integrated density is low ($\approx 1 \times 10^{20}$ m^{-2}) and comparable to plasma scenarios in MAST, which, instead, were characterized by strong chirping TAEs [17]. A possible explanation for this behavior might be the smaller spatial gradients in the fast ion distribution resulting from the combination of on-axis and off-axis heating, as well as from the smaller off-axis fast ion population for the same NBI input power, making discharge #45238 more similar to single-NBI plasma discharges in MAST [7] where both

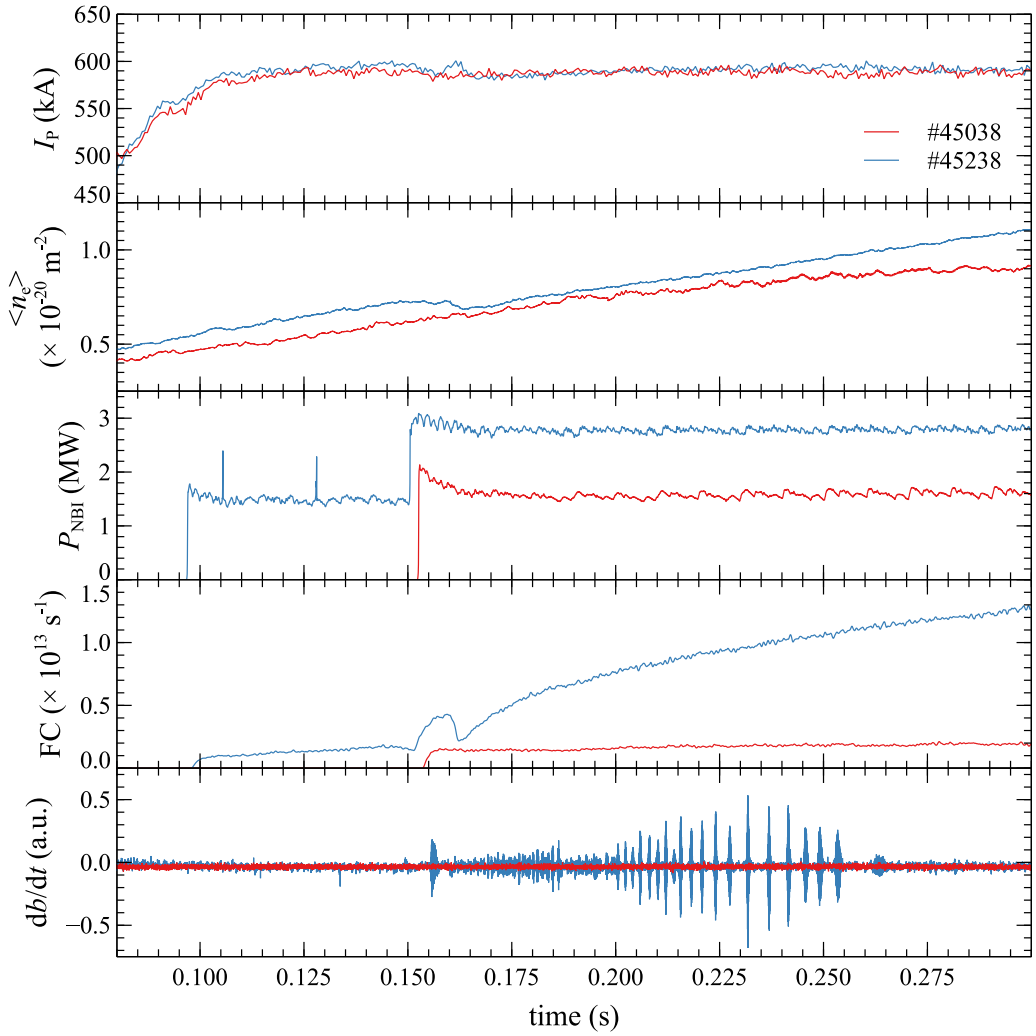

Figure 10. Comparison between two similar plasma discharges with only off-axis (#45038, red) and with both on-axis and off-axis NBI heating (#45238, blue). From top-to-bottom: plasma current, line integrated electron density, total NBI input power, FC neutron rate and magnetic perturbation.

NBIs were depositing fast ions in the plasma core: bursting TAEs were often accompanied by spikes in the D_α emission when both NBIs were used [29] but rarely when only one was used.

Figure 12 shows the global plasma parameters for pulse #45163 in which FBs and LLM are both present. This is an L-mode plasma with a flat-top plasma current of 450 kA in a double null conventional divertor configuration with low density and on-axis NBI heating with only 1.4 MW input power. In the early phase of the plasma discharge, when the on-axis safety factor decreases from an initial value of $q(0) \approx 3$, small amplitude TAEs can be observed. At around $t = 0.3$ s in the discharge, $q(0) \approx 1.1$ and a large amplitude FB occurs with a frequency chirping down from 40 to 10 kHz in the laboratory frame of reference. A large drop in the neutron rate is observed simultaneously on the FC and NCU. Following this, the fast ion population increases again in the core, giving rise to two more, small amplitude FBs until $q(0) \approx 1.0$ at $t = 0.35$ s, at which point an LLM appears, lasting for most of the NBI heating phase (no ST occurs in this phase). This behavior is confirmed by the spectrogram of the FILD signal shown at the bottom of figure 12, where both FBs and LLM can be observed, together with the simultaneous increase in the intensity of fast ion losses (continuous black line). Figure 13 shows in detail the evolution of the neutron rate profile during the FB on a 1 ms timescale. As the amplitude of the FB grows, the neutron profile begins to drop and flatten in the core, before developing a hollow-profile, indicating a large loss of fast ions. In the late phase of the FB, the fast ion population begins to recover and the neutron rate profile becomes core-peaked again, although at a lower level. The overall change in the fast ion density due to the FB is approximately −20% with a reduction as large as −35% in the core region (at around $p = 0.9$ m), as shown in the profile labeled (d) in the bottom panel of figure 13. The drop in the neutron rate during the FBs is entirely due to the loss of fast ions since the electron and temperature profiles are unchanged during the MHD perturbation burst. The FB impact on fast ions observed in MAST-U is quite similar to the one in MAST [29, 30]. During the LLM phase, the fast ion population drives the growth of the

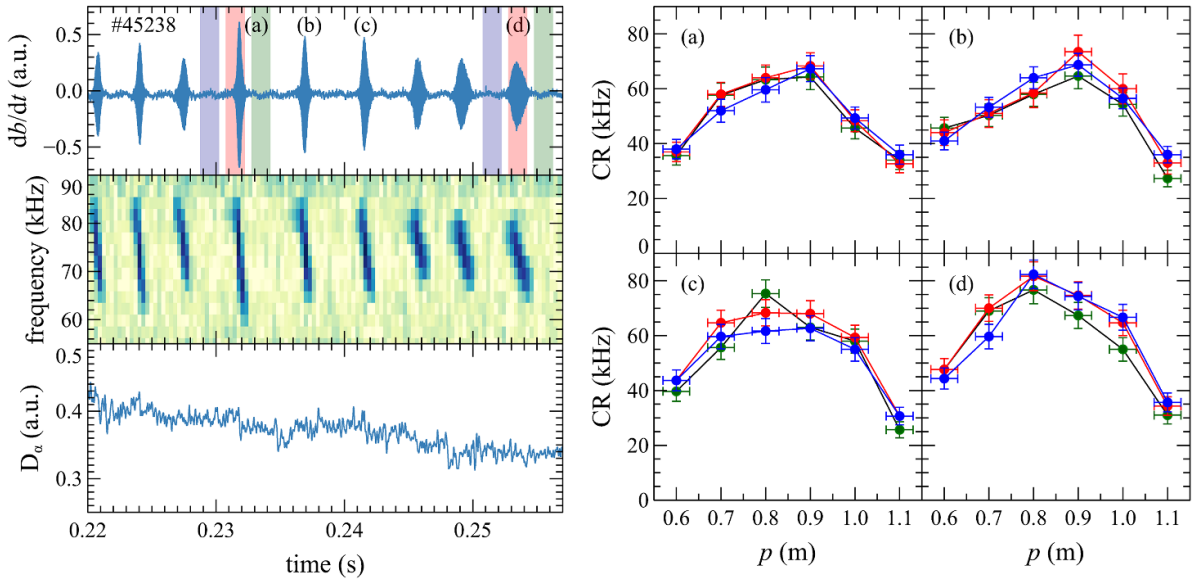

Figure 11. On the left, a closer look at the TAEs for pulse #45238: zoomed in view of the magnetic perturbation shown in figure 10, its spectrogram and the edge D_α photon recombination emission. On the right: neutron emissivity profiles for four TAEs (labeled (a)–(d)) before (blue), during (red) and after the chirping of the mode in the time intervals indicated in the corresponding color on the top panel on the left (shown for (a) and (d) only for clarity).

LLM until a maximum amplitude is reached, after which a decrease is observed in both the OMAHA and NCU rate profiles, as shown in figure 14. The overall reduction in the fast ion population inferred from the NCU measurements is approximately 15% of the pre-LLM phase across the entire plasma region. As the LLM decreases in amplitude, the neutron rate starts to recover to pre-maximum-LLM values, although it peaks more on the inboard side ($p = 1.0$ m). The reduction in the fast ion pressure gradient during the LLM is confirmed by a reduction in the core electron temperature and density from 2.8×10^{19} m^{-3} to 1.9×10^{19} m^{-3} and from 1.1 keV to 0.8 keV, respectively, resulting from the flattening of the profiles in a region 60 cm wide centered around the magnetic axis. As observed in [29], the reduction in the electron temperature and density profiles in itself is not sufficient to reduce the simulated neutron rate to the observed values, indicating that it is indeed related to the loss of fast ions. The reduction of the fast ion population observed in the LLM phase of this pulse is much smaller than those reported in MAST [29]. The most likely explanation is that in MAST-U, and in this plasma discharge in particular, the driving mechanism for TAEs, FBs and LLMs is weaker than in MAST due to the fact that these are driven by the on-axis NBI only, that is, by a much smaller fast ion population in the core to start with. In addition, the non-optimal performance of the on-axis NBI resulted in a full-energy fraction of the injected fast ions to be approximately half of the corresponding one in MAST plasmas with one NBI heating only.

An estimate of the radial gradient of the fast ion distribution $\partial f_{\rm fi}/\partial r$ for these discharges has been carried out using TRANSP/NUBEAM, assuming no fast ion anomalous diffusion. As in [17], the radial gradient of the fast ion distribution has been calculated at the probable location of the modes (at the normalized poloidal flux coordinate $\psi_{\rm n} \approx 0.4$ corresponding to the radial coordinate $r = 1.2$ m) at $t = 0.25$ s into the discharge. The results, shown in table 1, are compared to those calculated in [17] for low density pulses #29921 (two NBIs) and #29222 (one NBI), categorized as having $\partial f_{\rm fi}/\partial r$ greater than the threshold for no fast ion redistribution, and for high density pulses #29245 (2 NBIs) and #29195 (1 NBI) for which $\partial f_{\rm fi}/\partial r$ is below that threshold. Pulses #29222 and #45238 have comparable electron densities and $\partial f_{\rm fi}/\partial r$ as well as similar MHD activity, despite #45238 being a two-NBI discharge. For comparison, pulse #29921 was characterized by a much stronger MHD activity and larger $\partial f_{\rm fi}/\partial r$. Plasma discharge #45163, characterized by FBs, has a very low density and quite a large $\partial f_{\rm fi}/\partial r$ comparable to that of pulse #29976, which is a two-NBI discharge but with a much higher electron density. A preliminary interpretation of these observations is that (a) the off-axis NBI itself does not drive TAEs or energetic particle modes; (b) the combination of on- and off-axis NBIs indeed reduces the drive for fast ion MHD instabilities; and (c) the low densities in #45163 and #45238 compensate for the smaller fast ion population, providing just enough free energy to drive these instabilities. These results are consistent with the overall picture of fast ion distribution being driven by the combined effect of low plasma density and high NBI input power thanks to the synergetic effects discussed in detail in [17].

4.3. NCTMs

Figure 15 shows the time evolution of the global parameters for pulse #45006, an L-mode plasma with a flat top plasma current of 750 kA in a double null conventional divertor configuration and with an on-axis heating of 1.5 MW. The line integrated electron density increases throughout the plasma discharge, reaching a maximum value of $\approx 3 \times$

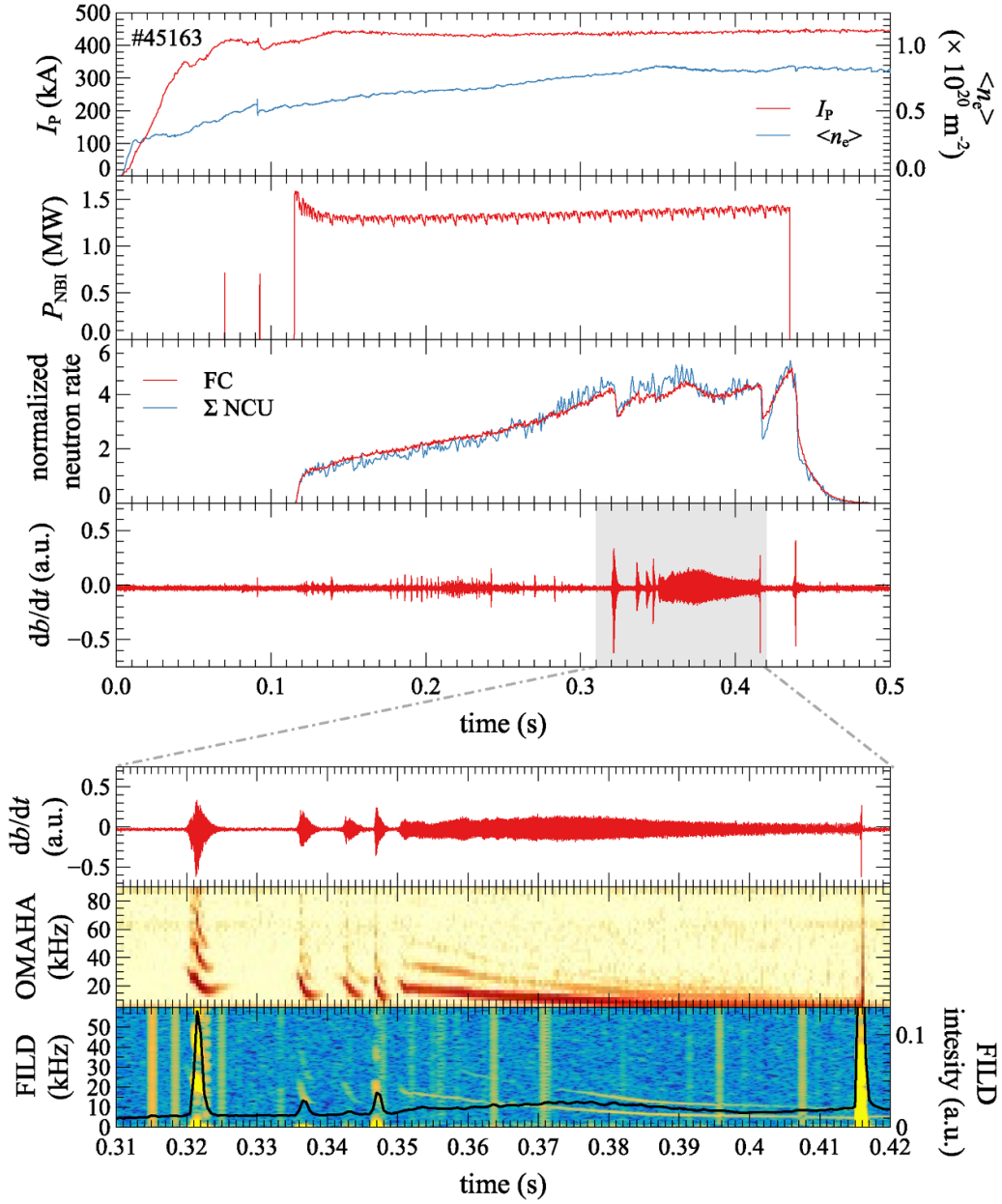

Figure 12. Global plasma parameters for plasma discharge #45163 characterized by FBs and LLM. From top-to-bottom: plasma current and line integrated electron density, NBI heating power, normalized neutron count rate measured by FC and NCU (sum over all channels), magnetic perturbation measured by an OMAHA coil. The gray region is expanded in the bottom figure showing details of the FBs and LLM together with the corresponding spectrogram and the FILD fast camera spectrogram with the fast ion loss intensity as a black line.

$10^{20}\,\mathrm{m}^{-2}$, while the on-axis safety factor is always $q(0) > 1$ reaching $q(0) = m/n = 2/1$ at about $t = 0.26$ s and approaching $q(0) = m/n = 3/2$ at about $t = 0.4$ s. The TAEs activity in this pulse is quite weak and limited to $t < 0.25$ s: in addition, short bursts of low frequency infernal modes are observed at around $t = 0.24$ s. The spectrogram of an OMAHA pick-up coil clearly show a perturbation appearing at around $t = 1.9$ s with an approximately constant frequency of 5 kHz, which, at the transition time $t = 0.37$ s, suddenly jumps to a frequency of ≈7.5 kHz which then decays slowly to its original value. The rotation frequency of the C^{5+} impurity for $r = 0.98$ m (plasma core) is also shown in the spectrogram: a strong reduction in the rotation frequency is observed as $q(0)$ approaches $(m,n) = 3/2$ for then matching the perturbation frequency. Around the transition time, the core electron temperature does not change but its radial profile becomes flatter, suggesting the formation of a magnetic island in the core with a width of approximately 30 cm, as shown in figure 16.

Later in the discharge, the core temperature is reduced to about 0.8 keV but the flattened profile is retained. Similarly, the core electron density does not change after the transition time and its radial profile flattens at the core value across a large part of the plasma volume. Later in the discharge, contrary to the electron temperature, the density increases and its profile becomes centrally peaked and quite broad. Due to the limited number of Mirnov coils that were available in the first

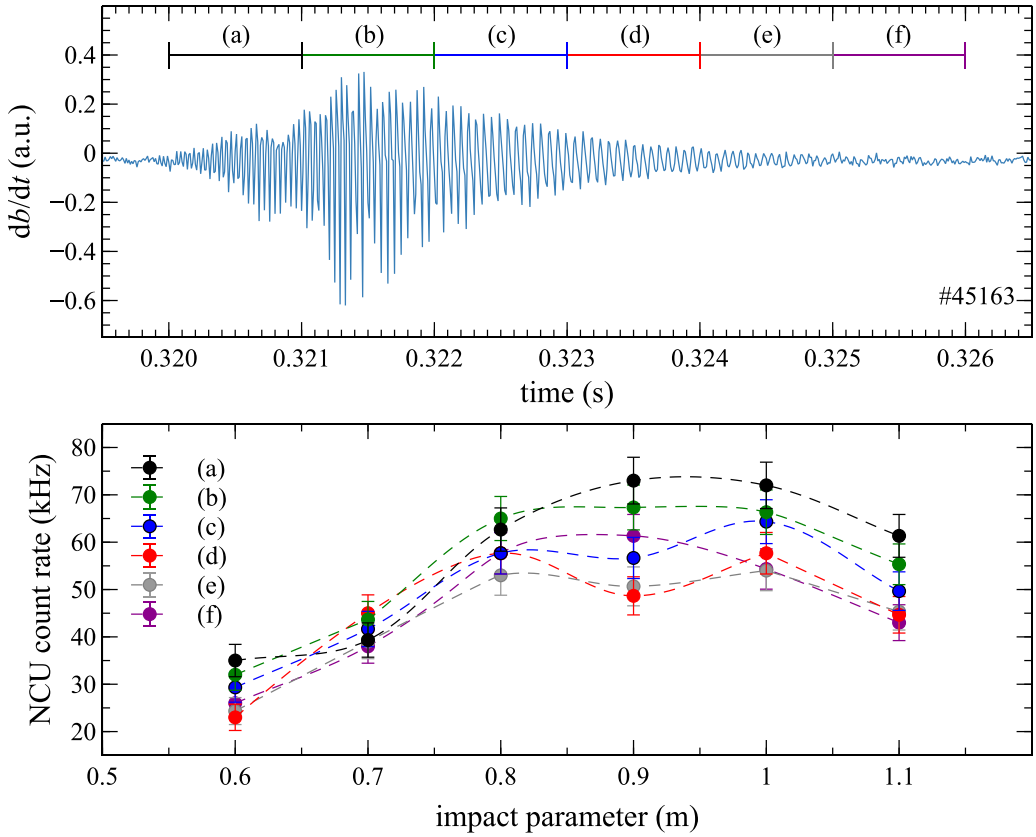

Figure 13. Time evolution of the magnetic perturbation during the FB at $t = 0.32$ for pulse #45163 (top panel) and of the neutron count rate profile (bottom panel) time integrated in the time intervals (a)–(f).

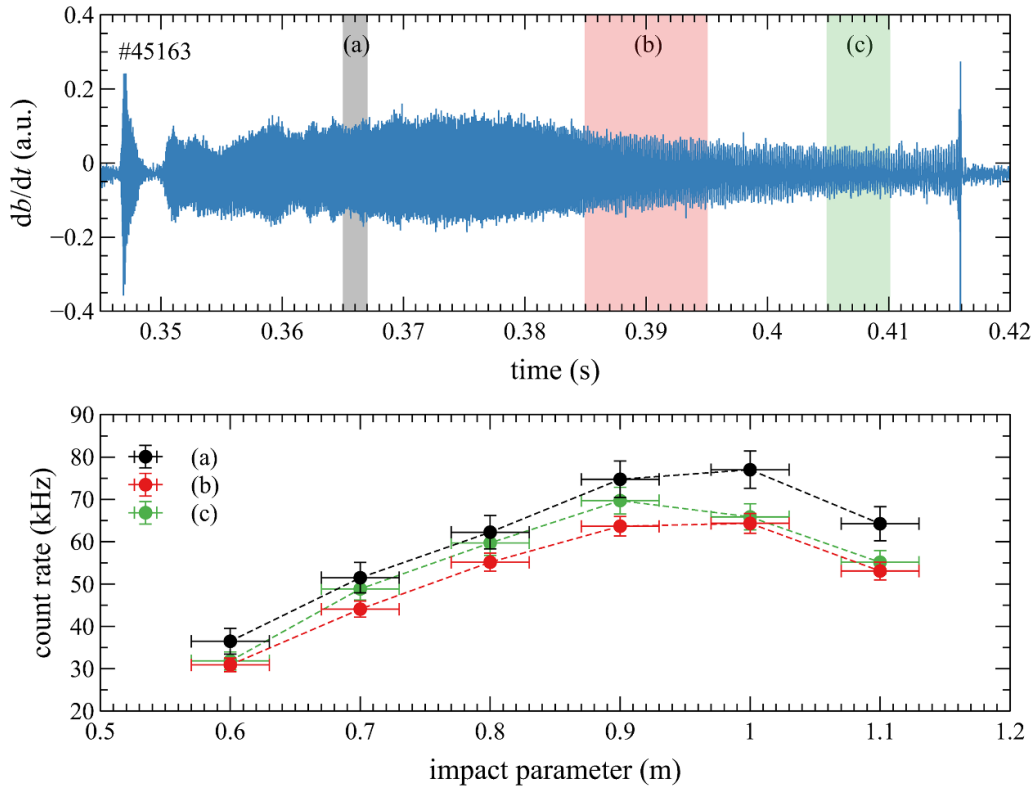

Figure 14. Time evolution of the magnetic perturbation during the LLM for pulse #45163 (top panel) and of the neutron count rate profile (bottom panel) measured at the times indicated by the colored areas.

Table 1. Radial gradients of the fast ion distribution for MAST and MAST-U pulses at $t = 0.25$ s and radial location $r = 1.2$ m.

Pulse #	$\partial f_{\rm fi}/\partial r$ (a.u.)	$< n_{\rm e} >$ $(\times 10^{20})$ m^{-2}	NBI configuration	MHD instability
29195	−1.6	2.10	on-axis	None
29245	−3.5	2.20	on-axis × 2	Weak FBs
29921	−9.0	1.12	on-axis × 2	Strong TAEs, FBs activity
29922	−3.4	1.05	on-axis	Weak TAEs, FBs activity
29976	−6.7	1.53	on-axis × 2	Medium TAEs, FBs, LLM
45163	−4.7	0.68	on-axis	Weak TAEs, medium FBs, LLM
45238	−2.5	0.95	on-axis + off-axis	Medium TAEs

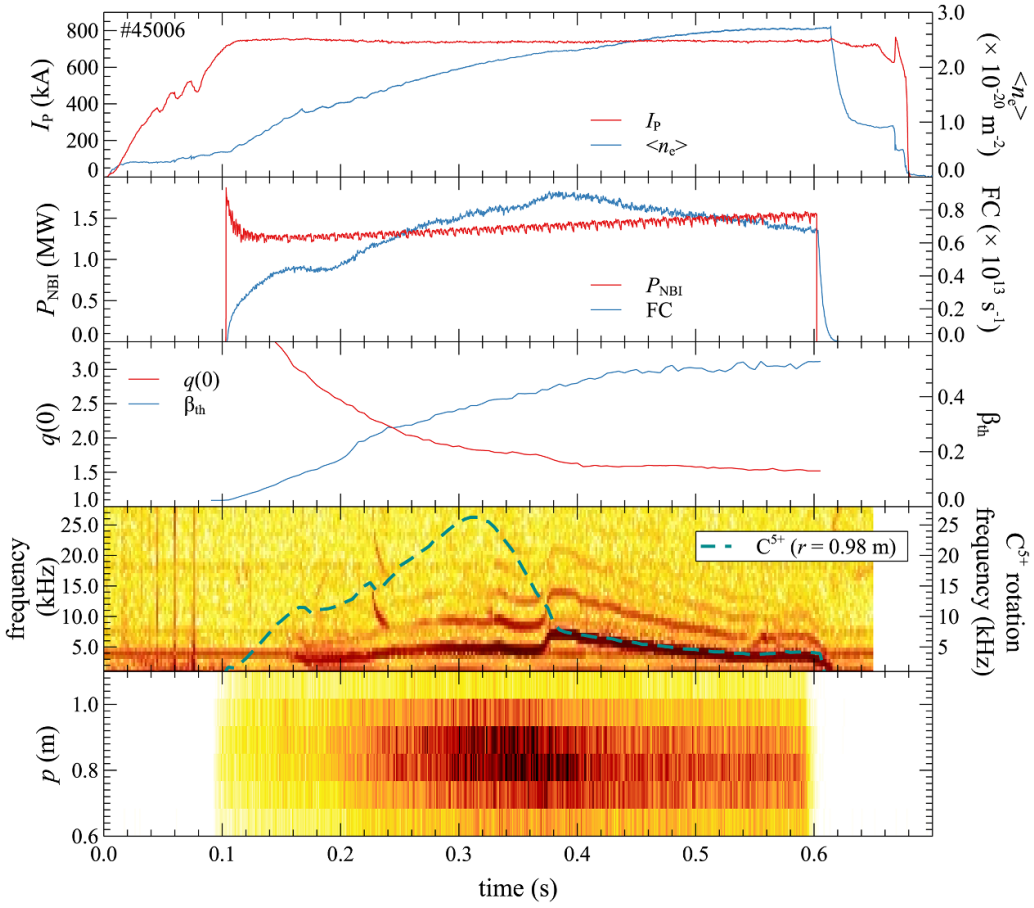

Figure 15. Global plasma parameters for plasma discharge #45006 characterized by NTMs. From top-to-bottom: plasma current and line integrated electron density, NBI heating power and count rate measured by the FC, on-axis safety factor and $\beta_{\rm th}$, spectrogram of OMAHA pick-up coils together with the C^{+5} impurity rotation frequency on-axis and the NCU count rate profile.

MAST-U experimental campaign, the mode number of the perturbation could not be determined. However, on the basis of the on-axis safety factor estimated by EFIT++, it is suggested that the observed perturbations are NTMs with mode numbers $(m,n) = 2/1$ and $(m,n) = 3/2$, respectively. The appearance of the NTMs is compatible with the evolution of $q(0)$, especially when allowing for the unavoidable uncertainties in the equilibrium reconstruction. The normalized thermal poloidal $\beta_{\rm th}$ (the ratio of thermal energy to the poloidal magnetic field energy) calculated by EFIT++ and shown in the middle panel of figure 15, reaches values similar to those observed in MAST discharges in which NTMs were present [31]. It is worth noting that the plasma discharge here discussed is quite different from the previous studies in MAST (L-mode versus H-mode and q-profile to name just a few). In particular, ST was identified as the triggering mechanism for NTMs in MAST [31], while in this case, there is a lack of a clear precursor which resembles observations reported in NSTX of triggerless NTMs [32]. At the transition time, the neutron rate, which was constantly growing, begins to decrease at a constant rate. This is clearly visible in the FC and NCU: in particular, in the latter, the peak of the profile moves inward after the onset of the $(m,n) = 3/2$ NTM, as shown in the bottom right panel of figure 16. TRANSP/NUBEAM simulations reproduce quite

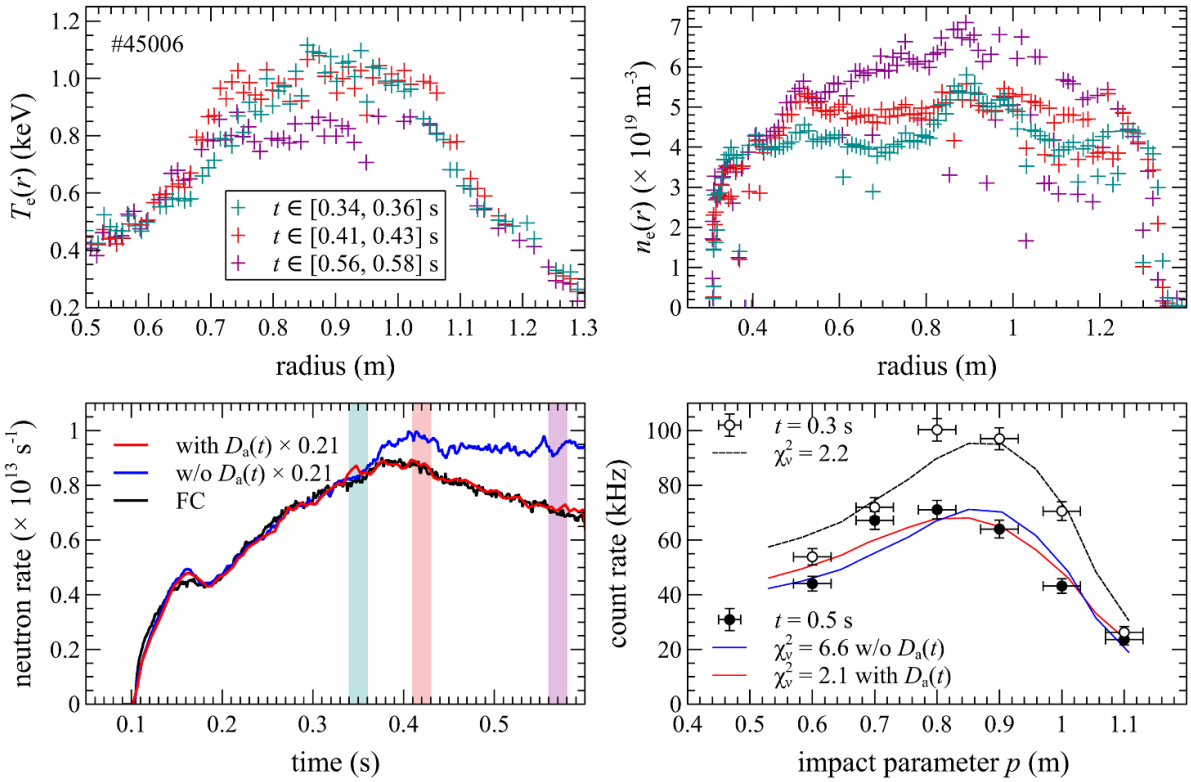

Figure 16. Top row: electron temperature and density before (cyan) and after (red) the onset of the $(m,n) = 3/2$ NTM. Bottom left: TRANSP/NUBEAM simulation of the total neutron rate measured by the FC (black) with (red) and without (blue) fast ion anomalous diffusion (the simulated rates have been scaled to match the FC rate in the early phase of plasma discharge #45006). Bottom right: comparison between measured (in black) and predicted NCU profiles with and without (red) and without (blue) fast ion anomalous diffusion of 3.6 m^2 s^{-1} at $t = 0.5$ s.

well the evolution of the neutron rate measured by the FC up to the transition time, but fast ion anomalous diffusion is required to match the experimental neutron rate, as shown in the bottom left panel of figure 16 (note that the predicted neutron rate in this figure has been scaled to match the FC neutron rate for $t \leqslant 0.37$ s). The required fast ion anomalous diffusion increases from 0.3 m^2 s^{-1} to 5.2 m^2 s^{-1} in the time interval 0.36 s–0.6 s. The inclusion of fast ion anomalous diffusion also provides a better agreement with the neutron rate profile measured by the FC. While β_{th} remains constant during the $(m,n) = 3/2$ NTM phase thanks to the increase in density compensating the drop in temperature, the reduction in the neutron rate is a clear indication of a reduction in the fast ion population in the core.

5. Conclusions

The NCU was designed to measure the neutron emissivity profile at six radial positions simultaneously with a time resolution of 1 ms and a statistical uncertainty of 10% in MAST-U scenarios with up to 10 MW of NBI input power. As shown in this study, the design requirements have been met already in the first MAST-U experimental campaign with only 3 MW of total input power. This has been achieved via an improved collimation and shielding as well as improved discrimination between neutrons and γ-rays. In particular, the predicted fast ion distribution with on-axis and off-axis NBI has been experimentally verified via TRANSP/NUBEAM simulations coupled to experimental measurements of the neutron emissivity profiles provided by the NCU. The good qualitative agreement found, without the need to recur to fast ion anomalous diffusion, provides an encouraging basis for the development of MAST-U operating scenarios at higher plasma current, toroidal field and NBI input power with a significant non-inductive current drive fraction. The quantitative comparison between NCU and FC measurements with TRANSP/NUBEAM simulations is still under investigation and it is likely that a combination of factors, such as the lack of effective charge Z_{eff} measurements and the uncertainty regarding the energy fractions of the on-axis NBI, might be the major contributors to the observed discrepancies. In order to address these issues, neutron activation foil measurements have also been carried out in MAST-U: the results and implications are the subject of a separate study.

The examples presented in this work of TAEs, FBs, LLMs, NTMs and ST testify to the rich fast ion physics phenomenology that can be studied in MAST-U. Losses of fast ions are predominant in the presence of FBs, LLMs, NTMs and STs, while TAEs result mainly in their redistribution. In particular, this study reports the first observation of weak amplitude perturbations reminiscent of ST which suppress the fast ion population in the core. The nature of this perturbation is not clear at this stage. It is worth mentioning

that in addition to TAEs, compressional Alfvén eigenmodes (CAEs) and global Alfvén eigenmodes (GAEs) have also been observed in MAST-U by both OMAHA and FILD diagnostics with associated fast ion losses [33]. The mechanism responsible for such losses, however, has not been fully identified yet as CAEs and GAEs occur simultaneously to ST. Further investigations will be carried out with dedicated experiments in the next MAST-U experimental campaign.

The impact of the combination of on- and off-axis NBI heating in reducing the radial gradient of the fast ion distribution, thus suppressing the energy source driving TAEs and energetic particle modes, has been investigated. The preliminary results indicate that, indeed, $\partial f_{\rm fi}/\partial r$ has a lower value in two NBI-heated plasma discharges, even compared with MAST plasma discharges with only one NBI source. The fact that the plasma discharge investigated in MAST-U has an even lower density than those studied in MAST reinforces the overall picture of the beneficial effect of a broader spatial deposition of fast ions.

Data availability statement

The data generated and/or analysed during the current study are not publicly available for legal/ethical reasons but are available from the corresponding author on reasonable request.

Acknowledgments

This work has been carried out within the framework of the EUROfusion Consortium, funded by the European Union via the Euratom Research and Training Programme (Grant Agreement No. 101052200 - EUROfusion). Views and opinions expressed are, however, those of the author(s) only and do not necessarily reflect those of the European Union or the European Commission. Neither the European Union nor the European Commission can be held responsible for them. This work has been carried out with the support of the RCUK Energy Programme (Grant No. EP/T012250/1) and of the Swedish Research Council (VR) Grant No. 2021-05485.

ORCID iDs

M Cecconello https://orcid.org/0000-0002-2571-1920
A Sperduti https://orcid.org/0000-0002-9911-1549
J Rivero-Rodriguez https://orcid.org/0000-0001-5074-0267

References

[1] Gorelenkov N N, Pinches S D and Toi K 2014 *Nucl. Fusion* **54** 125001
[2] McClements K G and Fredrickson E D 2017 *Plasma Phys. Control. Fusion* **59** 053001
[3] Morris W *et al* 2014 *IEEE Trans. Plasma Sci.* **42** 402
[4] Scanell R *et al* 2022 *48th EPS Conf. Plasma Physics* (Maastricht) p O1.104
[5] Gee S J *et al* 2005 *Fusion Eng. Des.* **74** 403–7
[6] Homfray D A *et al* 2009 *IEEE 2009 23rd IEEE/NPSS Symp. Fusion Engineering - SOFE (San Diego, CA)* pp 1–4
[7] Turnyanskiy M, Challis C D, Akers R J, Cecconello M, Keeling D L, Kirk A, Lake R, Pinches S, Sangaroon S and Wodniak I 2013 *Nucl. Fusion* **53** 053016
[8] Rivero-Rodriguez J F *et al* 2018 *Rev. Sci. Instrum.* **89** 10I112
[9] Perez R V *et al* 2014 *Rev. Sci. Instrum.* **85** 11D701
[10] Cecconello M *et al* 2014 *Nucl. Instrum. Methods Phys. Res.* A **753** 72
[11] Cecconello M Sperduti A, Fitzgerald I, Conroy S, Holm S J and Weiszflog M 2018 *Rev. Sci. Instrum.* **89** 10I110
[12] Scannell R Walsh M J, Dunstan M R, Figueiredo J, Naylor G, O'Gorman T, Shibaev S, Gibson K J and Wilson H 2010 *Rev. Sci. Instrum.* **81** 10D520
[13] Conway N J , Carolan P G, McCone J, Walsh M J and Wisse M 2006 *Rev. Sci. Instrum.* **77** 10F131
[14] Hole M J , Appel L C and Martin R 2009 *Rev. Sci. Instrum.* **80** 123507
[15] Goldston R J , McCune D C, Towner H H, Davis S L, Hawryluk R J and Schmidt G L 1981 *J. Comput. Phys.* **43** 61
[16] Pankin A, McCune D, Andre R, Bateman G and Kritz A 2004 *Commun. Comput. Phys.* **159** 157
[17] Keeling D L *et al* 2015 *Nucl. Fusion* **55** 013021
[18] Klimek I Cecconello M, Gorelenkova M, Keeling D, Meakins A, Jones O, Akers R, Lupelli I, Turnyanskiy M and Ericsson G 2015 *Nucl. Fusion* **55** 023003
[19] Cecconello M Boeglin W, Keeling D, Conroy S, Klimek I and Perez R V 2019 *Nucl. Fusion* **59** 016006
[20] Hirvijoki E Asunta O, Koskela T, Kurki-Suonio T, Miettunen J, Sipilä S, Snicker A and Äkäslompolo S 2014 *Comput. Phys. Commun.* **185** 1310–21
[21] Asunta O Govenius J, Budny R, Gorelenkova M, Tardini G, Kurki-Suonio T, Salmi A and Sipilä S 2015 *Comput. Phys. Commun.* **188** 33–46
[22] Sperduti A Cecconello M, Conroy S and Snicker A 2021 *Nucl. Fusion* **61** 016028
[23] Cecconello M Sperduti A 2018 *Plasma Phys. Control. Fusion* **60** 055008
[24] Jackson A R *et al* 2020 *Nucl. Fusion* **60** 126035
[25] Kim D Podestá M, Liu D and Poli F M 2018 *Nucl. Fusion* **58** 082029
[26] Liu D Heidbrink W W, Podestá M, Hao G Z, Darrow D S, Fredrickson E D and Kim D 2018 *Nucl. Fusion* **58** 082028
[27] Kim D Podestá M, Liu D, Hao G and Poli F M 2019 *Nucl. Fusion* **59** 086007
[28] Podestá M Gorelenkova M, Gorelenkov N N, White R B, Bonofiglo P J, Poli F M, Teplukhina A, Yang J, Cecconello M and Vallar M 2022 *Plasma Phys. Control. Fusion* **64** 025002
[29] Cecconello M *et al* 2015 *Plasma Phys. Control. Fusion* **57** 014006
[30] Jones O M *et al* 2015 *Plasma Phys. Control. Fusion* **57** 125009
[31] Buttery R J , Sauter O, Akers R, Gryaznevich M, Martin R, Warrick C D, Wilson H R and MAST Team T 2002 *Phys. Rev. Lett.* **88** 125005
[32] Gerhardt S P *et al* 2009 *Nucl. Fusion* **49** 032003
[33] Rivero-Rodriguez J *et al* 2022 *48th EPS Conf. Plasma Physics* (Maastricht) p O4.109